

# Wall-Less Flow Phantoms With Tortuous Vascular Geometries: Design Principles and a Patient-Specific Model Fabrication Example

Chung Kit Ho, Adrian J. Y. Chee, *Graduate Student Member, IEEE*, Billy Y. S. Yiu, *Member, IEEE*, Anderson C. O. Tsang, Kwok Wing Chow, and Alfred C. H. Yu, *Senior Member, IEEE*

**Abstract**—Flow phantoms with anatomically realistic geometry and high acoustic compatibility are valuable investigative tools in vascular ultrasound studies. Here, we present a new framework to fabricate ultrasound-compatible flow phantoms to replicate human vasculature that is tortuous, nonplanar, and branching in nature. This framework is based upon the integration of rapid prototyping and investment casting principles. A pedagogical walkthrough of our engineering protocol is presented in this paper using a patient-specific cerebral aneurysm model as an exemplar demonstration. The procedure for constructing the flow circuit component of the phantoms is also presented, including the design of a programmable flow pump system, the fabrication of blood mimicking fluid, and flow rate calibration. Using polyvinyl alcohol cryogel as the tissue mimicking material, phantoms developed with the presented protocol exhibited physiologically relevant acoustic properties [attenuation coefficient:  $0.229 \pm 0.032$  dB/(cm · MHz) and acoustic speed:  $1535 \pm 2.4$  m/s], and their pulsatile flow dynamics closely resembled the flow profile input. As a first application of our developed phantoms, the flow pattern of the patient-specific aneurysm model was visualized by performing high-frame-rate color-encoded speckle imaging over multiple time-synchronized scan planes. Persistent recirculation was observed, and the vortex center was found to shift in position over a cardiac cycle, indicating the 3-D nature of flow recirculation inside an aneurysm. These findings suggest that phantoms produced from our reported protocol can serve well as acoustically compatible test beds for vascular ultrasound studies, including 3-D flow imaging.

**Index Terms**—Design principle, patient-specific model fabrication, tortuous vascular geometry, wall-less flow phantom.

## I. INTRODUCTION

FLOW phantoms are well recognized as essential laboratory tools in the field of vascular ultrasound [1]. These experimental test beds, consisting of a vascular lumen

Manuscript received September 16, 2016; accepted December 2, 2016. Date of publication December 6, 2016; date of current version January 11, 2017. This work was supported in part by the Natural Sciences and Engineering Council of Canada (RGPIN-2016-04042), Canada Foundation for Innovation (36138), Hong Kong Innovation and Technology Fund (ITS/150/15), and Research Grants Council of Hong Kong (GRF 785113M).

C. K. Ho, A. J. Y. Chee, and B. Y. S. Yiu are with the Department of Electrical and Electronic Engineering, The University of Hong Kong, Hong Kong.

A. C. O. Tsang is with the Department of Surgery, The University of Hong Kong, Hong Kong.

K. W. Chow is with the Department of Mechanical Engineering, The University of Hong Kong, Hong Kong.

A. C. H. Yu is with the Department of Electrical and Computer Engineering, University of Waterloo, Waterloo, ON N2L 3G1, Canada (e-mail: alfred.yu@uwaterloo.ca).

Digital Object Identifier 10.1109/TUFFC.2016.2636129

model and a flow circuit, have conventionally been used as calibration platforms for clinical ultrasound scanners [2] and as training devices in vascular diagnostics education [3]. From the perspective of fostering technology development, flow phantoms may also serve as investigative tools for the testing of novel vascular ultrasound techniques [4], [5]. Indeed, in lieu of simulation analyses [6], [7], which can only evaluate the algorithmic performance of vascular ultrasound techniques, flow phantom studies can practically support the testing of hardware prototypes, and, in turn, yield performance insights that incorporate system-level efficacy considerations. Furthermore, in contrast with *in vivo* investigations where the actual hemodynamics are typically not well understood, flow phantom experiments allow the performance of vascular ultrasound algorithms to be systematically assessed under controllable and known flow conditions.

In constructing flow phantoms for use in the development of vascular ultrasound technologies, straight tube geometries [8], [9], rotating cylinders [10], [11], and string models [12] are perhaps the simplest types that have been realized. These models are not difficult to fabricate, but their configuration is a substantial deviation from the human vascular anatomy. Thus, ultrasound images and measurements taken on these phantoms characteristically lack resemblance of observations acquired under *in vivo* settings. In order for phantom experiments to yield performance findings that are relevant to *in vivo* conditions, it is necessary to design vascular models with anatomically realistic geometries [1]. On this topic, previous efforts have made use of multi-stage investment casting principles to construct generalized carotid bifurcation [13] and renal artery models [14] that are co-planar in nature, and some versions have incorporated a vessel wall feature [15], [16]. This fabrication technique has also been extended to create aortic aneurysm models [17] and nonplanar vascular models with mild geometric curvatures [18], [19]. Nonetheless, these prior endeavors have generally stopped short of producing complex vascular models with multiple tortuous vessel branches and nonplanar pathological features. From a technical standpoint, such a lack of progress is seemingly attributed to: 1) cumbersomeness in making a negative mold with tortuous parting lines as needed for complex lumen core fabrication and 2) difficulty in divesting the tortuous lumen replicate material after phantom construction.

Alternatively, flow phantoms with more complicated vascular geometries may be built through direct application of addi-

tive manufacturing or rapid prototyping principles [20], [21]. In the context of vascular ultrasound research, this approach has been realized in the forms of numerically controlled milling [22] and stereolithography [23] to construct carotid bifurcation phantoms with multiple disease features (stenotic narrowing and plaque ulceration). There has also been success in using rapid prototyping techniques to directly develop intracranial aneurysm models [24]. Despite being convenient, the existing rapid prototyping protocols for ultrasound flow phantom fabrication have one technical drawback: that is, the material used for rapid prototyping (whether plastic or photopolymer) typically has mediocre acoustic compatibility, including speed of sound mismatch and high acoustic attenuation [22], [23]. This drawback makes it difficult to obtain good ultrasound signal quality from these flow phantoms.

Here, we present a new engineering protocol for developing ultrasound-compatible flow phantoms with tortuous vascular lumen (and indeed, any arbitrary geometry). This new framework has overcome the technical drawbacks of previous solutions that made use of direct rapid prototyping (i.e., poor acoustic compatibility) and investment casting (i.e., difficulty in making negative molds for tortuous lumens and divesting the corresponding lumen replica). Its conceptualization is built upon our methodological assertion that rapid prototyping and investment casting, despite their individual drawbacks, can be rationally integrated, such that the technical benefits of both approaches can be harnessed to develop tortuous vascular flow phantoms with high ultrasound compatibility. In doing so, performance assessment of emerging vascular ultrasound methods can be effectively facilitated, especially high frame rate imaging solutions that are rapidly maturing in recent years [25]–[29]. Indeed, since tortuous vessels are non-planar in nature, the phantoms developed using our new protocol can also be useful to 3-D flow imaging investigations [30], [31].

In this paper, a patient-specific intracranial aneurysm model is leveraged as an exemplar demonstration of our new tortuous phantom design framework. This model was chosen not only because ultrasound-compatible cerebral aneurysm phantoms have not been reported previously, but also because this diseased vasculature is marked by tortuous vascular branches and non-planar disease features [32], [33]. Within this context, we shall provide a pedagogical walkthrough of our vascular lumen model development protocol. In addition, we shall present a laboratory procedure for constructing a supporting flow circuit that does not rely on commercial flow pump systems, and we shall show a series of flow imaging results taken using our developed phantoms. It should be noted that our protocol is intended for developing flow phantoms that are wall-less: a technical characteristic that is well acknowledged as being suitable for vascular ultrasound investigations unless arterial wall dynamics are the subject of analysis [8].

## II. TORTUOUS PHANTOM DESIGN PROTOCOL

### A. Overview of Design Protocol

Our protocol generally involves the following steps. First, a computer-aided design (CAD) model of the tortuous vasculature is created based on an arbitrary vascular geometry or a

medical imaging data set (such as a CT data volume) obtained from a patient. After adding supporting components, such as flow connectors to the CAD model, a physical replicate of this model is fabricated with 3-D printing tools. Next, the vasculature replicate is mounted onto a phantom box, and polyvinyl alcohol (PVA) cryogel is casted around the replicate to mimic surrounding tissues. Subsequently, multiple freeze and thaw cycles are administered for the cryogel to congeal. At last, the embedded replicate is removed by submersing the tissue slab in a chlorinated solvent, creating a void that resembles the vessel lumen. Details on the specific steps of this protocol are described in the following subsections.

### B. CAD Model Drafting for Tortuous Vascular Geometry

1) *Patient-Specific Model for Tortuous Vasculature:* The cerebrovascular geometry used as the case example in the presentation of our new tortuous phantom design protocol was acquired from a 60-year female volunteer who has been diagnosed with intracranial aneurysm development at the intersection between the distal internal carotid artery (ICA) and the middle cerebral artery (MCA). A 128-slice CT angiogram scan protocol (using Iopamiro 370 contrast) was used to obtain the image volume of the patient's cerebral vasculature. The research use of this scan data was consented by the patient, and the protocol was approved by the Institutional Review Board of the University of Hong Kong/Hospital Authority Hong Kong West Cluster. The acquired CT image volume was stored in digital imaging and communications in medicine (DICOM) format. Note that the CT image's grayscale value at a given pixel was essentially mapped to its locally measured Hounsfield unit.

2) *CAD Model Generation:* As an initial step of creating an ultrasound-compatible tortuous phantom from the patient's CT data set, a CAD model of the 3-D cerebrovascular geometry was constructed using the Mimics software (Materialise NV, Leuven, Belgium). In approaching this task, we first loaded the CT image volume into Mimics [Fig. 1(a)], and for each image slice, the vascular region was identified through the use of a vascular segmentation mask that isolated image grayscale values greater than a predefined threshold. Next, a volumetric rendering of the tortuous vasculature was generated by stacking together the vascular-masked CT slices and applying a smoothening function to the resulting image stack [Fig. 1(b)]. From this 3-D rendering, we extracted and isolated the bifurcation section where the aneurysm was located at the intersection between ICA, MCA, and a third posterior communicating artery (PCA) branch. A 3-D mesh volume was then generated for this aneurysm-bearing bifurcation, and the result was saved in stereolithography (STL) file format [Fig. 1(c)] to facilitate further amendments in a CAD software. Note that, for this patient-specific cerebrovascular geometry, the vessel diameter for the three artery branches was, respectively, measured to be 5.6 mm (ICA), 2.7 mm (MCA), and 1.6 mm (PCA).

### C. Physical Fabrication of Tortuous Vasculature Model

1) *CAD Model Refinements for Phantom Construction:* In the next stage of phantom development, a physical replicate

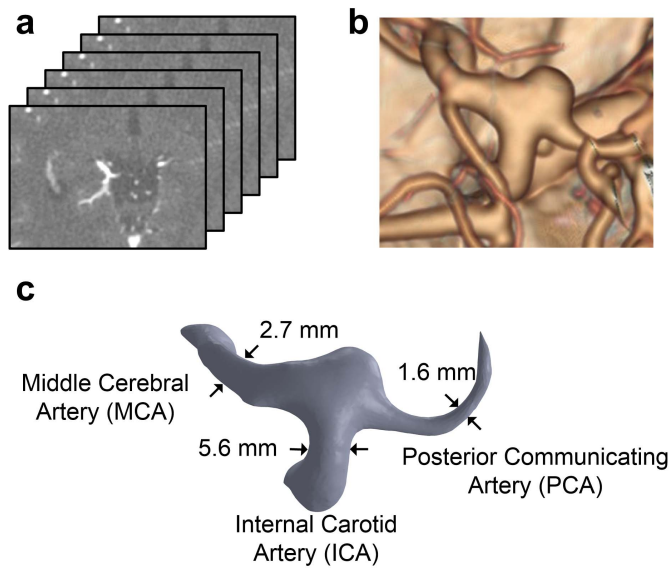


Fig. 1. Example of tortuous vascular geometry construction using patient-specific imaging data. (a) Cerebral CT slices (stored in DICOM format) with vascular regions highlighted using Iopamiro 370 contrast were acquired from a subject with cerebral aneurysm. (b) Using the Mimics software, a 3-D rendering (with surface smoothing) of the tortuous vascular lumen was generated from the CT image volume. (c) Cerebral aneurysm and its three main vessel branches (MCA, ICA, and PCA) were manually extracted, and its corresponding 3-D mesh volume was exported as an STL file.

of the tortuous vascular geometry was constructed using 3-D printing tools that operated upon fused deposition modeling principles. In preparation for this process, two technical features were added to the CAD model of the tortuous vasculature. First, size-matched cylindrical flow connectors were added to the ends of branches in the vascular geometry. In our patient-specific cerebral aneurysm example, these flow connectors were attached to the inlet branch (ICA) and the two outlet branches (MCA and PCA). Such a task was realized by: 1) loading the STL file of the CT-derived bifurcation geometry into the SolidWorks software (Dassault Systemes, Waltham, MA, USA) and 2) using CAD drafting functions available in SolidWorks to append cylindrical pipes to the three ends of the cerebrovascular model [Fig. 2(a)]. The second technical feature that was added to the vascular CAD model was the affixing of the tortuous vasculature to a supporting cylinder that served as a structural scaffold when the model was printed. The vasculature and the supporting cylinder were joined by adding connecting branches, as indicated in Fig. 2(b). The modified CAD model was then saved as a new STL file.

2) *Compilation of 3-D Printing Instructions:* The STL file of the modified vascular CAD model as described earlier was next loaded into an open-source KISSlicer software (ver. 1.5) to compile 3-D printing machine instructions in G-code format. For this process, the vasculature and its accompanying supporting cylinder were first aligned in an upright position. Subsequently, the layer thickness and the skin thickness were, respectively, set to 0.1 and 0.3 mm, and a 12.5% infill percentage was specified to produce vascular replicates with partial interior void, such that they become physically

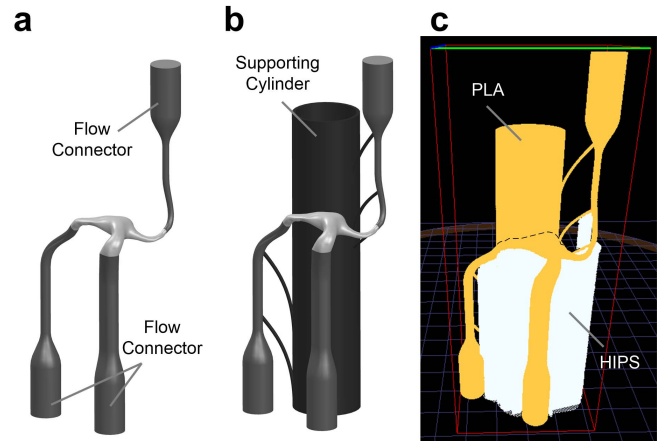


Fig. 2. Key steps involved in the creation of a tortuous vascular CAD model for 3-D printing. (a) Flow pipes and connectors were first appended to the inlet and outlet of the aneurysm model. (b) Vasculature was then affixed to a central supporting cylinder that served as a structural scaffold. (c) Using the KISSlicer software, a supporting base was added to the model during print instruction compilation. The vascular model and the supporting base were, respectively, built using PLA and HIPS as the 3-D printing materials.

breakable (an essential feature leveraged during vessel core removal in the investment casting process; see Section II-D). Also, as a preventive measure against mechanical collapsing of the developing replicate during fused deposition, a supporting base was added to the print instructions by activating the support options in KISSlicer [Fig. 2(c)].

3) *Overview of 3-D Printing Process:* The compiled G-code instructions were downloaded to an open-source 3-D printer with two material extruder channels (Model DX; CreatBot 3-D Printer, Zhengzhou, China) to build the physical replicate of the tortuous vasculature. The extruder head size was 0.25 mm, and this value practically represents the print resolution of each layer for the vascular replicates developed using our protocol. Polylactic acid (PLA) was used as the build material for the vasculature, and it was fed from the 3-D printer's first material extruder channel. In contrast, high-impact polystyrene (HIPS), as fed from the printer's second extruder channel, was used to build the supporting base. It is worth noting that two of PLA's material properties—(i) insolubility in water and limonene and (ii) dissolvability in chlorinated solvents—are of particular relevance to our phantom construction process (to be described later in this section). For our cerebral aneurysm case example, its raw completed 3-D printer output is shown in Fig. 3(a).

4) *Extraction of Vascular Replicate:* After the 3-D printing process was completed, the tortuous vasculature replicate was extracted as follows. First, the supporting base (printed using HIPS material) was dissolved by immersing the raw 3-D printer output in a limonene solvent (62122; Sigma-Aldrich, St. Louis, MO, USA) for 12 h. A photo of the remaining PLA structure (after rinsing with tap water) is shown in Fig. 3(b). The supporting cylinder was then removed from the tortuous vasculature replicate by cutting the connecting branches using an ultrasonic knife



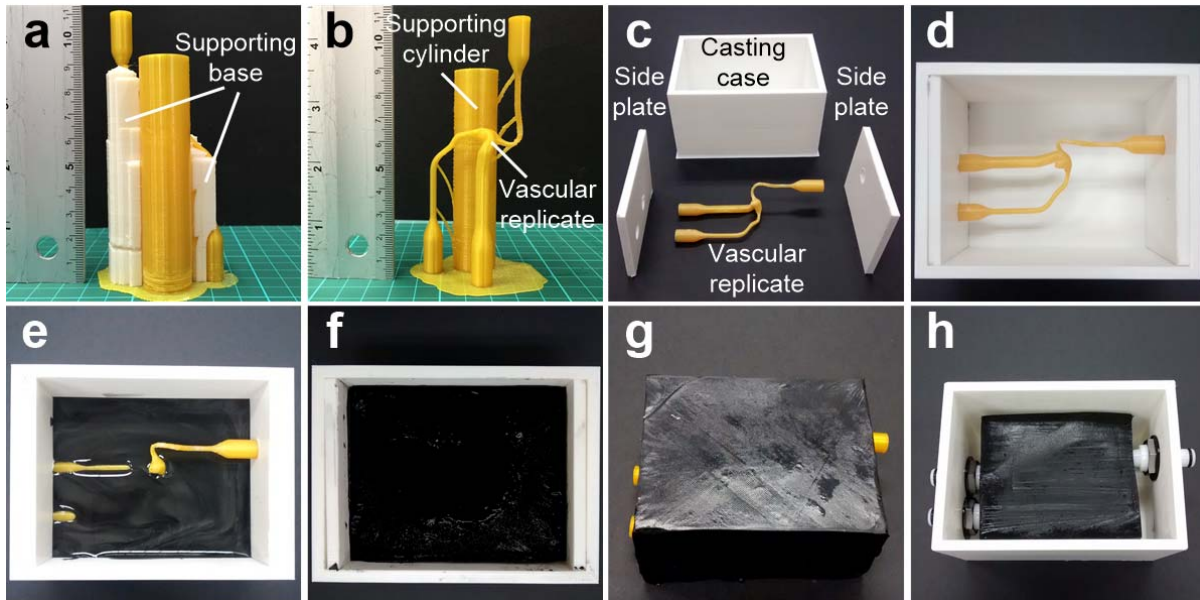


Fig. 3. Photographic depiction of various steps in tortuous phantom development. (a) Raw 3-D printer output with the main PLA structure (yellow) and the HIPS supporting base (white). (b) Vascular replicate along with the supporting cylinder after removing the HIPS supporting material. (c) Key hardware components involved in phantom construction: casting case, two side plates, and the vascular replicate. (d) Mounting of the vascular replicate onto the two side plates and placed within the casting case cavity. (e) Casting case with the suspended vascular replicate and the cavity half-filled with PVA mixture. (f) Top-down view of the casting case filled with PVA mixture, embedding the vascular replicate within. (g) Replicate-containing tissue mimicking slab after the freeze-thaw procedure. (h) Completed phantom after removing the vascular replicate from the tissue mimicking slab and installing flow connectors.

(ZO-41; EchoTech, Aichi, Japan) and gently smoothening the cut points with sandpaper.

#### D. Casting of Tissue Mimicking Slab

1) *Casting Parts Construction*: To facilitate the construction of a tortuous vascular phantom using the 3-D printed vascular replicate, two side plates and a casting case were drafted using SolidWorks. The function of the two side plates was threefold: 1) to fasten either the inlet or outlet end of the vascular replicate within the casting case prior to tissue mimic casting; and 2) to facilitate vascular replicate removal after tissue mimic casting. On the other hand, the casting case served two functions: 1) to provide a well-defined volumetric cavity for tissue mimic casting and 2) to act as the phantom box after vascular replicate removal. For our cerebral aneurysm case example, the inner dimensions of our casting case were, respectively,  $81 \times 111 \times 60 \text{ mm}^3$  (length  $\times$  width  $\times$  height), and the thickness of each of its sides was 4 mm. Each side plate was  $81 \times 60 \text{ mm}^2$  (length  $\times$  width) in dimension and 4 mm in thickness. For the side plates and the two short sides of the casting case, three circular voids were created at positions corresponding to the inlet and outlet branches of the vascular replicate. After drafting the CAD models for these casting parts, they were fabricated as a PLA structure using the same 3-D printing method, as described in Section II-B, with the exception that a 100% infill percentage was specified here to produce nonporous casting parts. See Fig. 3(c) for a photo of the fabricated casting parts along with the vascular replicate prior to mounting. Note that, in this example, the casting parts were built using another PLA material color (white) to visually distinguish them from the vascular replicate (yellow).

2) *Mounting of Vascular Replicate*: In preparation for the tissue mimic casting process, the inlet and outlet ends of the vascular replicate were fastened onto the corresponding side plate. After that, the two side plates were slid into the casting case and were aligned against the short side walls of the case, as shown in Fig. 3(d). Pressure-sensitive adhesive (Blu-tack; Bostik SA, Paris, France) was then placed at the common edge between each side plate and the corresponding short side wall of the case to prevent the side plate from moving out of position during tissue mimic casting.

3) *Polyvinyl Alcohol Mixture Preparation*: To facilitate the formation of an elastic tissue mimicking slab that more closely resembles tissue elasticity, a PVA cryogel mixture was prepared at  $90 \text{ }^\circ\text{C}$  using these constituent materials: 1) 10% (by weight) PVA powder (341584; Sigma-Aldrich); 2) 3% fine graphite particles (282863; Sigma-Aldrich); 3) 0.3% potassium sorbate preservatives (85520; Sigma-Aldrich); and 4) 86.7% distilled water. After cooling this mixture for 12 h (to foster degassing), it was poured slowly into the casting case's volumetric cavity where the vascular replicate was suspended within [see Fig. 3(d) and (e)]. Gas bubbles arising at the mixture surface were gently removed using a baking scraper. A sheet of cling wrap was then placed at the top of the casting case to help maintain equilibrium of the PVA mixture.

4) *Freeze Thaw of PVA Mixture*: Three cycles of freezing and thawing were applied to develop the cryogel properties of the PVA mixture in the casting case. For each freezing step, the entire casting case was placed in a  $-20 \text{ }^\circ\text{C}$  freezer for 24 h; as for each thawing step, the casting case was placed within a  $4 \text{ }^\circ\text{C}$  refrigerator for 24 h. It is known that the PVA

molecules within the mixture would form polymer crystallites during the freezing step, and these crystallites would form porous networks to yield elastic material characteristics during the thawing step [34].

### E. Extraction of Vascular Replicate

1) *Removal From Casting Case*: In the final stage of our tortuous phantom design protocol, the vascular replicate (now embedded within the PVA tissue mimicking slab) was eliminated to vacate a void that corresponds to the tortuous vascular lumen. In approaching this task, we first took the tissue mimicking slab out of the casting case by: 1) gently flipping the casting case upside down and 2) sliding out the side plates and the tissue slab that were sandwiched together. After that, the two side plates were removed to leave behind the replicate-containing tissue mimicking slab, a photo of which is shown in Fig. 3(g).

2) *Immersion in Chloroform*: To dissolve the vascular replicate and in turn vacate the vascular lumen void, the tissue mimicking slab was immersed within chloroform (372978; Sigma-Aldrich), which is a chlorinated solvent that can dissolve PLA material without affecting the hydrous PVA cryogel. Note that, in accordance with proper safety practice, this step was conducted inside a chemical fume hood. The chloroform immersion was allowed to take place for 10 min, after which the tissue mimicking slab was taken out, and its surface and lumen were rinsed with distilled water.

3) *Reattachment to Phantom Box*: After removing the vascular replicate, the tissue mimicking slab was reinserted into the casting case that was being reused as a phantom box. Prior to performing this reinsertion step, a sheet of 5-mm-thick rubber was placed at the inner bottom side of the phantom box to absorb ultrasound pulse transmissions when performing imaging experiments. Also, quick-fit flow-tube connectors (EW-06361-61; Cole-Parmer, Vernon Hills, IL, USA) were installed onto the circular voids on the side walls of the phantom box to enable connection with the flow circuit during operations. See Fig. 3(h) for a photo of the completed tortuous phantom, where the tissue mimicking slab with vascular lumen void was mounted onto the phantom box.

## III. FLOW CIRCUIT CONSTRUCTION PROCEDURE

### A. Overview of Flow Pump System

1) *Hardware Components*: To drive the operations of the tortuous vascular phantoms that we developed using our engineering protocol, it is not necessary to rely on commercial flow pump systems. Instead, we have built an in-house programmable flow pump system that can allow the flow pulse shape and the flow rate to be customized. Our flow pump system was developed using six major components: 1) direct-current (DC) power supply (S-400-36; StepperOnline Co. Ltd., Nanjing, China); 2) gear pump (PQ-12; Greylor Co., Cape Coral, FL, USA); 3) servo motor (YZ-57BLS140; Yizhi Technology Ltd., Hangzhou, China); 4) motor driver (YZ-ACSD608; Yizhi); 5) Arduino board (Mega 2560; Adafruit Industries,

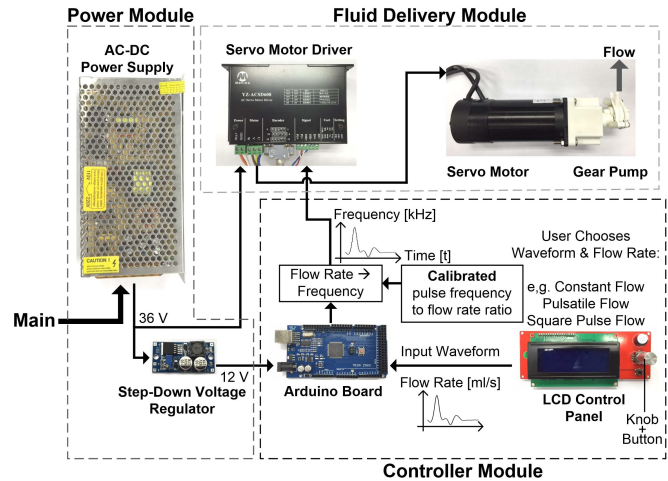


Fig. 4. Key components of the flow pump assembly, categorized into three modules: power, controller, and fluid delivery. See Section III-A2 for description of the system’s operations.

Manhattan, NY, USA); and 6) liquid crystal display input–output (I/O) panel (2004 Smart LCD Controller; SainSmart, Lenexa, KS, USA). These components are interconnected, as shown in Fig. 4. They were essentially organized in three major modules: power, controller, and fluid delivery.

2) *System Operations*: In our flow pump system, the power module (equipped with a power supply that can feed 36 V maximum DC voltage and 400-W maximum power output) was responsible for supplying dc voltage to the motor driver and the Arduino board, which, respectively, operated at 36 and 12 V. Since the required rail voltage of these two terminal loads was not the same, a step-down voltage regulator (LM2596HV module; Shenzhen Leading Chips, Shenzhen, China) was used to downscale the power supply voltage to the level required for the Arduino board, while the 36 V output from the power supply was connected directly to the motor driver. With this power feed, the other two modules in our flow pump system operated as follows. First, in the Fluid Delivery module, the motor driver was responsible for commanding the run-time behavior of the servo motor (and, in turn, the gear pump) through the use of three “motor” pins on the driver board. While the exact signals delivered from these “motor” pins were set internally within the driver board, their temporal dynamics were externally manipulated through two input pins (“pulse” and “direction”) that were connected to the respective signal output pins of the Arduino board. In the controller module, user input was provided to the Arduino board through the I/O panel, where the user was allowed to choose a preset flow waveform pattern (constant, square, and pulsatile) and specify the flow rate (from 0–30 mL/s). With these inputs, the Arduino board was programmed using the C language to derive the pump driving signals (“pulse” and “direction”) and to relay them to the motor driver. The procedure for such derivation operation shall be described in the next subsection.

3) *Flow Rate Calibration and Control Algorithm*: The flow rate driven by the fluid delivery module was controlled via a

series of pulses generated by the controller module through the “pulse” pin. For every pulse that was received, the gear pump would rotate by 1/1000 revolution; the flow rate can, therefore, be increased by sending pulses at a higher frequency from the controller module (the rate at which impulses delivered to control flow rate is hereafter referred as the pulsing frequency). To alter the pulsing frequency, Arduino board was set to operate in the fast pulsewidth modulation mode, such that the pulsing rate would be updated instantaneously to match the desired flow rate. As well, flow direction was controlled by pulling the “direction” pin high for forward flow and vice versa.

Calibration of the relationship between pulsing frequency and flow rate was performed by measuring the amount of blood mimicking fluid (BMF) delivered by the gear pump over a fixed time period (repeated for different pulsing frequencies). For this task, the controller module was set to operate for 30 s at a fixed pulsing frequency, and BMF was drawn from the fluid reservoir by the gear pump with the outflow directed to a measuring cylinder. The fluid flow volume was recorded, and the flow rate (measured flow volume divided by 30 s) was calculated accordingly for that particular pulsing frequency. This measurement procedure was repeated with pulsing frequencies ranging from 5 to 70 kHz at an interval of 5 kHz to obtain different flow rate values. Subsequently, a calibration curve was obtained by plotting the measured flow rate as a function of pulsing frequency, and a linear relationship was observed between the two (data not shown). Linear regression was then performed over the data set to determine the pulse-frequency-to-flow-rate coefficient, which was found to be equal to  $2.32 \text{ kHz/mL} \cdot \text{s}^{-1}$  ( $R^2 = 0.998$ ). Note that this linearity trend can be safely assumed in general, because the gear pump specifications have indicated less than 5% deviation in flow rate for a 5 psi (259 mmHg) pressure head.

For the flow pump system to drive a preset flow waveform (such as pulsatile flow in carotid), their flow velocity profiles were first coded in the program. These waveforms were described by 100 sample points of instantaneous flow velocity whereby each flow rate was converted to its corresponding pulsing frequency based on the linear model obtained through empirical calibration. The update rate to the pulsing frequency generated by the controller module was set based on the simulating heart rate (user-defined beats per minute) to update the pulsing frequency 100 times within a cardiac cycle.

4) *User Interface*: Our pump system included an LCD display panel and a knob button to control its operation. Their I/O operations were controlled by the Arduino board’s software with calls to the corresponding library functions. To configure the flow profile, i.e., flow waveforms, peak flow rate, and heart rate, the knob was turned to: 1) alternate between selections and 2) adjust the values of each selected parameter. All flow parameters were displayed on the LCD panel during operation.

5) *Synchronization With Image Acquisition*: To help track the pulsatile flow cycle phase during ultrasound imaging

experimentation, our flow pump system has included a synchronization feature that would send an external trigger pulse at the start of each preset waveform pulse (disabled when the pump operates in constant flow conditions). The trigger pulse was generated by configuring a digital output pin of the Arduino board to deliver a 10-ms burst pulse. It served to provide a temporal reference to the acquired image frames, akin to an electrocardiogram (ECG) gating function for *in vivo* investigations.

### B. Blood Mimicking Fluid Fabrication

The BMF used for the tortuous vascular phantoms was a standardized formula with acoustic scattering and viscosity properties matched to those of human blood [35]. We have refined the fabrication procedure to make it more accessible to academic laboratories with basic wet-lab facilities and the necessary raw materials. The key stages of the fabrication process are described as follows.

1) *Creation of a Dual-Chamber Filter Box*: Using CAD, the geometry of an open box was first created. This open box was consisted of a chamber well (6 cm) as well as a side hole for hose and screw placement [see Fig. 5(a)]. Two copies of the open box were then physically built using 3-D printing (described in Section II-B) with 100% infill percentage to prevent leakage. Afterward, the hole position of the two open boxes was aligned against each other, and a stainless steel mesh filter with  $33\text{-}\mu\text{m}$  pore size (316L; TWP Inc., California, USA) was sandwiched between them using two silicone sealing rings. In doing so, a dual-chamber filter box was assembled; the two chambers were, respectively, for hosting in-flow and out-flow BMF fabrication [see Fig. 5(b)].

2) *Flow Circuit Assembly for BMF Fabrication*: Four components were involved in the flow circuit for BMF fabrication: 1) a master fluid reservoir (essentially a plastic box); 2) the filter box as described in Section III-B1; 3) a gear pump as described in Section III-A to facilitate fluid circulation during BMF fabrication; and 4) connecting flow tubes (EW-96480-04; Cole-Parmer). A photo of the setup is shown in Fig. 5(c). During operation, the raw materials for BMF fabrication were added stepwise to the master reservoir (see Section III-B3), and the gear pump passed fluid from the reservoir through the filter box to sieve the raw BMF, and then back to the reservoir for further recirculation. To prevent large aggregates from forming within the filter box and to avoid particles from accumulating on the filter mesh, a magnetic stirrer was placed inside the in-flow chamber of the filter box, and the fluid was driven at 10 mL/s by the gear pump.

3) *Preparation of BMF Mixture*: Materials were added in the following order: 1) 83.7% (by weight) distilled water; 2) 0.3% potassium sorbate, which served as an antibacterial agent (85520; Sigma-Aldrich); 3) 3.3% dextran, which was required to tune the viscosity (D4876; Sigma-Aldrich); 4) 10.0% glycerol, which served to tune the acoustic speed and density (15514-029; Thermo Fisher Scientific, Waltham, MA, USA); 5) 0.9% Tergitol surfactants (86453; Sigma-Aldrich);



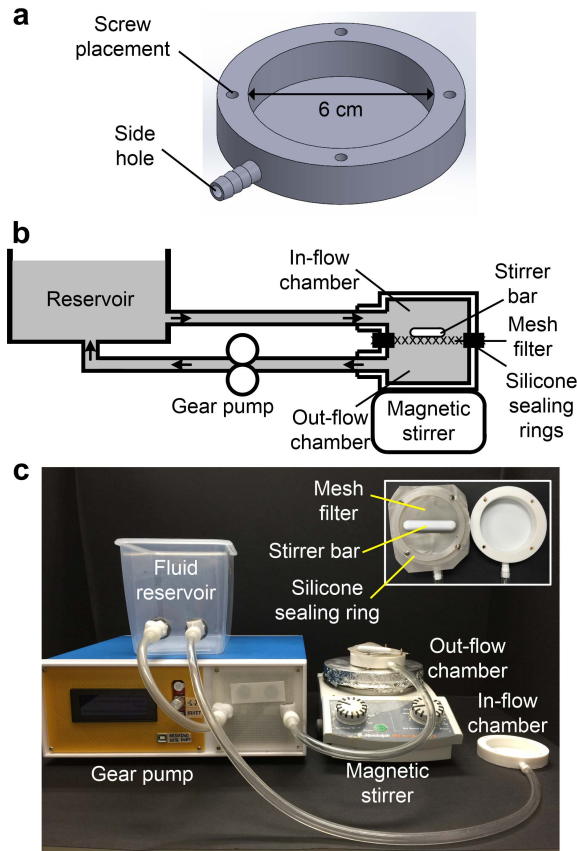


Fig. 5. Illustrations of dual-chamber filter box and setup for BMF fabrication. (a) CAD model for dual-chamber filter box (single side), with an inner diameter of 6 cm. Side holes are included as fluid inlet/outlet. (b) Diagram illustrating BMF fabrication setup. BMF ingredients were added to the reservoir during fabrication and drawn to the filter box by the gear pump, to sieve large aggregates with a metal mesh filter. A stirrer bar was placed in the in-flow filter chamber to break large aggregates. (c) Photograph of the actual setup for BMF fabrication. The top-right corner shows the mesh filter being sandwiched between two open boxes to form the dual-chamber filter box.

and 6) 1.8% Orgasol (2001 UD NAT1; Arkema, Paris, France), which served as acoustic scatterers of  $5 \mu\text{m}$  diameter.

4) *BMF Storage Prior to Use in Experiments*: After the BMF was mixed well, it was transferred to a bag using the gear pump, passing through the mesh filter to further remove clumps in the final mixture. This process was repeated twice to ensure no clump in the final mixture solution.

#### IV. CHARACTERIZATION OF PHANTOM PROPERTIES

##### A. Acoustic Compatibility

Acoustic speed and attenuation coefficient of tissue mimicking material were measured using the same insertion-based measurement technique previously described [23]. In brief, the setup comprised a pair of aligned transducers with test samples of varying thickness placed between them. During measurement, a 20-cycle pulse was transmitted for each frequency over the range of 3–7 MHz (in steps of 0.1-MHz increment), and the received signal was recorded to derive its acoustical properties.

Test slabs of different thicknesses (2, 4, 6, and 8 cm) were prepared by congealing PVA cryogel mixture in 3-D printed molds of their respective dimensions; a total of 120 test slabs were collectively fabricated (30 samples for each thickness). Three freeze-thaw-cycles were administered on each test sample, identical to the phantom fabrication procedure described in Section II.

The time-of-flight method [36] was applied to estimate the acoustic speed, similar to our earlier work [23]. In addition, amplitude thickness regression method [15] was adopted to derive the attenuation coefficient (with linear frequency dependence assumed based on published data [37]). The experimentally derived acoustic speed was  $1535 \pm 2.4 \text{ m/s}$ , which is close to the nominal speed of 1540 m/s for human tissue. The attenuation coefficient was found to be  $0.229 \pm 0.032 \text{ dB}/(\text{cm} \cdot \text{MHz})$ , which is relatively low compared with nominal attenuation coefficient of 0.3–0.7 dB/(cm · MHz). Taken together, these measurements suggest that the tissue mimicking material of our phantoms is compatible with ultrasound imaging experimentation.

##### B. Resemblance of Pulsatile Flow Patterns

To test the consistency of pulsatile flow patterns generated by our flow pump system, pulsed Doppler was performed to examine the generated flow profile. For this task, the flow pump was first connected to a straight rigid silicone tube of 9.6 mm inner diameter (EW-06411-12; Cole-Parmer), and flow was driven through this tube. Note that a rigid tube was used here to limit flow waveform distortions caused by vessel compliance. Doppler spectrograms (see Fig. 6) were then acquired using an ultrasound scanner with an L14-5 linear array transducer (SonixTouch; Analogic Ultrasound, Peabody, MA, USA) as previously described [23]. The transducer was aligned with the flow tube at 2.5 cm depth in long-axis view, and was tilted to achieve a beam-to-flow angle of 60, as shown in Fig. 6(a). A 4.5-mm range gate was placed at vessel center together with the transmit focus; transmit center frequency and pulse repetition frequency were 6.6 MHz and 1.7 kHz, respectively.

The flow pump was first configured to drive a constant flow rate of 10 mL/s through the flow setup. The corresponding Doppler spectrogram (after angle correction) is shown in Fig. 6(b). The maximum velocity, measured with the built-in function of the SonixTouch scanner, was found to be 27.1 cm/s, corresponding well to the 27.6-cm/s centerline peak velocity for a 10-mL/s flow rate passing through a 9.6-mm-diameter flow channel. In addition, the flow velocity profile remained similar throughout the entire acquisition, indicating that a stable constant flow was delivered by the flow pump system.

Next, the flow pump's custom flow waveform delivery function was evaluated. In our first test, the flow pump was configured to drive a 10-mL/s forward-flow profile modulated by a train of square pulses that switched between ON-and-OFF states at a rate of 2 Hz; these settings are equivalent to a 50% duty cycle square wave periodic signal over a one second interval (60 beats/min). Fig. 6(c) shows the corresponding

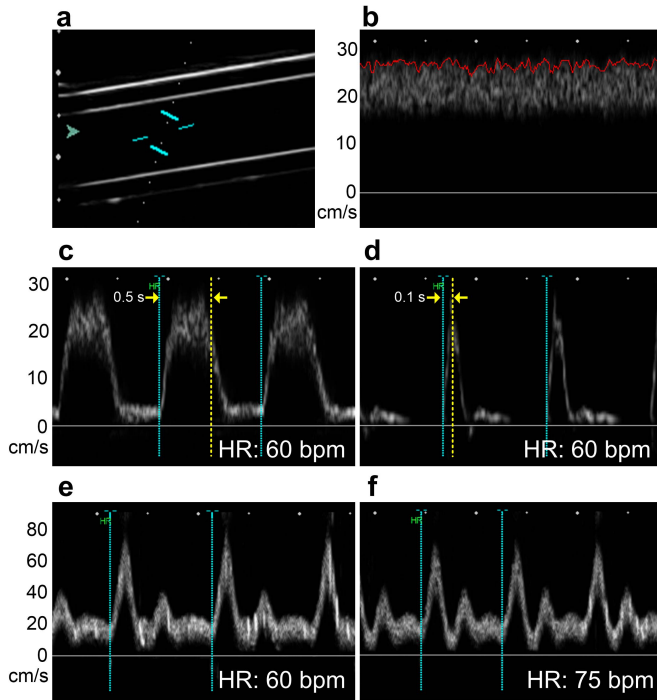


Fig. 6. Doppler spectrograms obtained from a rigid straight tube phantom with different flow pulse waveforms. (a) Pulsed Doppler range gate was placed at the vessel center of the flow tube. (b) Doppler spectrogram obtained from constant flow rate at 10 mL/s. Peak velocity was 27.1 cm/s. (c) and (d) Doppler spectrograms obtained from square pulse flow waveform at 10-mL/s peak flow rate and 60 beats/min; pump operating at duty cycles of (c) 50% and (d) 10%. (e) and (f) Doppler spectrograms obtained from carotid pulse waveform at 27-mL/s peak flow rate, at (e) 60- and (f) 75-beats/min pulse rate. The pulse rate of each flow waveform was measured using built-in heart rate measurement function in the ultrasound scanner, as indicated by the cyan-colored lines. (c)–(f) Measured heart rates were indicated at the bottom-right corner of each spectrogram.

Doppler spectrogram. A few observations of interest can be noted: 1) a maximum flow velocity of 27.1 cm/s was measured, and it was consistent with values obtained by both theoretical calculation and Doppler spectrogram of constant flow; 2) the matching measurement of beats/min using the clinical scanner’s built-in heart rate function [cyan lines in Fig. 6(c)] confirmed a precise temporal scheduling of our flow pump; and 3) the steep edges of the square waveforms indicate a low transient response when switching between states.

To test the pump’s ability to generate burst pulses, the duty cycle of the above 10-mL/s forward flow profile was reduced to 10% (ON-state of 0.1 s at 1-Hz pulse rate). The corresponding spectrogram is shown in Fig. 6(d). In this plot, the peak velocity at the flow tube center was observed to be the same as that in Fig. 6(c). To indicate the switch of states in Fig. 6(c) and (d), a yellow line was manually overlaid onto the spectrogram by measuring for equidistance between the cyan lines [for Fig. 6(c)] and one-tenth distance of the cyan lines [for Fig. 6(d)], respectively. The corresponding results showed that, despite the presence of a transient response, the peak velocity of 27.1 cm/s was attained within an ON-state of 0.1 s.

To demonstrate its configurability in driving arbitrary flow waveforms, the flow pump was set to deliver a

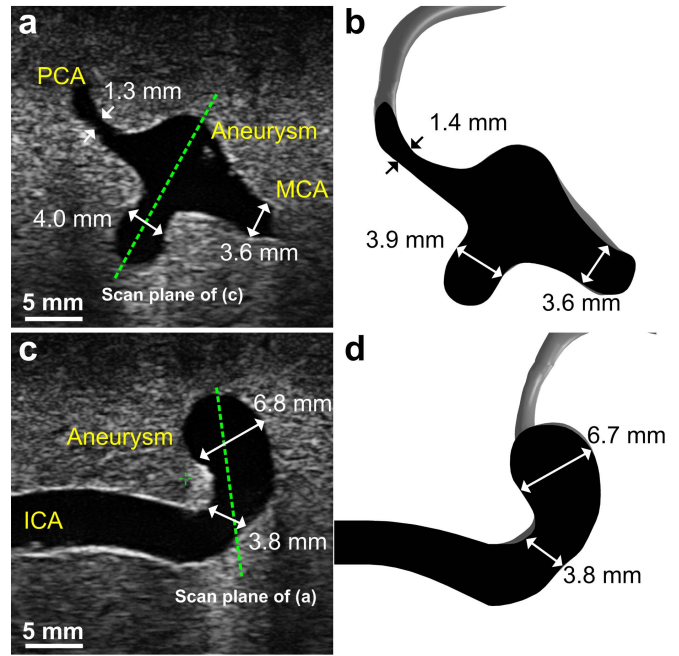


Fig. 7. Comparison of physical dimensions between tortuous vascular phantom and CAD model. Left column shows images taken from the flow phantom using clinical scanner; right column shows the same scan planes segmented from the CAD model. Images on the top row show the cross-sectional view of aneurysm, and MCA and PCA side branches; bottom row shows images obtained from the long-axis view of ICA inlet connected to the aneurysm. The orthogonal scan-plane positions are correspondingly marked as green lines in (a) and (c). The dimensions indicated on the left column were measured using the built-in distance function of the clinical scanner, while those on the right column were measured from the CAD software.

carotid flow profile. The flow rate at peak systole was set to 27 mL/s to mimic physiological flow scenario as reported [38]. Fig. 6(e) and (f) shows the Doppler spectrograms obtained from carotid pulse waveform with the heart rates of 60 beats/min (1 Hz) and 75 beats/min (1.25 Hz), respectively. Both spectrograms exhibited distinctive peak systole, dicrotic notch and dicrotic wave, all of which are key features for carotid pulse waveforms. The heart rates for the two pulse waveforms were gauged using the SonixTouch scanner’s built-in heart rate function. They were expectedly found to be consistent with the user-defined values.

### C. Resemblance of Tortuous Vessel Lumen

To confirm the vascular geometry of the fabricated tortuous flow phantom, B-mode images were acquired using the clinical mode of the SonixTouch scanner. The center frequency and line density were set to 6.6 MHz and 256 lines, respectively. Also, the vessel lumen of the phantom was connected to the programmable flow pump system that was feeding the same carotid flow output profile shown in Fig. 6(e), and images were acquired during diastole that corresponded to the baseline operational dimension. As shown in Fig. 7, two imaging planes were selected (left column) for comparison with the same planes from the CAD model (right column). The top row shows the cross-sectional view of the aneurysm that was located at the junction between PCA and MCA; the bottom row shows the long-axis view of ICA inlet connecting to the



aneurysm. As shown in Fig. 7(a), the luminal diameter for ICA inlet and PCA and MCA outlets at these positions was 4, 1.3, and 3.6 mm, respectively (measured using the built-in distance function of the SonixTouch scanner). These values were in line with the CAD model dimensions of 3.9, 1.4, and 3.6 mm for ICA, PCA, and MCA, respectively [see Fig. 7(b)]. A similar trend can be observed for the long-axis ICA image plane shown in Fig. 7(c) and (d). In general, an insignificant measurement difference of  $\pm 0.05$  mm (from 15 measurements) was observed between the lumen dimensions of the phantom and the CAD model.

## V. PHANTOM OPERATION AND EXPERIMENTATION

### A. Flow Circuit Assembly

Our flow phantom was put into operation by connecting it to the flow pump system as follows. First, the phantom's ICA inlet branch was connected to the outlet of flow pump using a flexible vinyl flow tubing attached with quick-fit connectors. Next, two 2-mm-diameter flow resistors were connected on both PCA and MCA outlet branches before the flow conduits merge to a Y-junction connector, channeling flow back to the flow pump reservoir. Upon assembling the flow circuit, the flow pump was configured to drive the preset carotid pulse flow profile at 1.25 Hz (i.e., 75 beats/min). The mean and systolic pump outputs were 1.82 and 6.5 mL/s, respectively.

### B. Plane Wave Imaging Experimentation





To visualize flow dynamics within the tortuous vascular phantom, plane wave imaging was performed to acquire images at high frame rates beyond the video display range. This was achieved using our group's research-purpose ultrasound imaging platform that comprised a reconfigurable transmit pulser based on the research mode of our SonixTouch scanner and a channel-domain data acquisition unit [39]. During data acquisition, the transmit pulser was programmed to send plane wave pulses in sequence from three steering angles ( $-10^\circ$ ,  $0^\circ$ , and  $10^\circ$ ) by adjusting the transmit delays for each of the 128 elements. The center frequency, pulse duration, and PRF were, respectively, set to 5 MHz, 3 cycles, and 10 kHz. For each transmission, raw channel-domain data were acquired over all 128 array elements up to 5 cm depth on a consecutive basis until the hardware's onboard data buffer was filled. Note that our system was equipped with 16 GB of memory, and it was sufficient to store up to 2.5 s of channel-domain data sampled at 40 MHz at 12-bit resolution. The channel data were then transferred to our graphical processing unit (GPU) platform [40] for offline processing, where analytic signal conversion and delay-and-sum beamforming were carried out. The image frames were constructed on a pixel-by-pixel basis (with  $0.1 \times 0.1$  mm<sup>2</sup> pixel dimension), leveraging on our previously established GPU-based beamformer [41] before performing Doppler analysis with MATLAB (MathWorks Inc., Natick, MA, USA) as described in Section V-C.

### C. Signal Processing for Color Encoded Speckle Imaging

Using the beamformed data frames from plane wave imaging, color-encoded speckle imaging (CESI) was performed

as an initial attempt to visualize complex flow dynamics within the cerebral aneurysm flow phantom. As described previously [26], CESI is a duplex visualization technique that renders complementary information on flow speed and flow trajectory, the latter of which is useful for determining flow direction in cases with Doppler aliasing. For this technique, its signal processing first involved summing a set of three-angle image frames to construct a high-resolution image (HRI). Note that the effective PRF has correspondingly reduced to one-third of its original value (3.3 kHz in this case). Subsequently, the HRIs were stacked along the slow-time domain to form a 3-D Doppler data matrix, and the slow-time ensembles for Doppler processing were formed from the set of analytic signal samples along the slow-time axis at each individual pixel position. Next, clutter suppression on each slow-time ensemble was performed using a 50-Hz cutoff frequency high-pass filter (134-tap, 100-dB suppression for equiripple criterion) to obtain the respective flow signal ensemble. After that, CESI frames were derived by: 1) extracting blood speckles based on instantaneous Doppler power and 2) estimating flow velocity using lag-one autocorrelation with a sliding-window approach (64 samples, slide by steps of one frame). These operations were executed individually at all pixels to generate flow speckle maps and flow velocity maps for all acquired frames, and a CESI cineloop was generated by compounding the flow speckle map onto B-mode images and overlaying flow velocity maps (with alpha compositing) at flow-detected regions. For reference, Doppler spectrograms were also generated by performing short-time Fourier transform (with 64-sample sliding window size) on the averaged slow-time ensemble of HRI pixels within a desired range gate. Note that the data overlap in between spectral estimates was 98.4%.

### D. CESI Visualization of Flow Inside Aneurysm Phantom

Four CESI cineloops acquired at different scan planes of the phantom are presented in  Movie 1 (nominal frame rate: 3333 frames/s and playback rate: 200 frames/s). The long-axis view of the aneurysm together with its ICA inlet is depicted on the top-left corner  Movie 1a) of the movies, while the three remaining  Movies 1b–1d) are acquired from the cross-sectional plane of the aneurysm (spaced by 0.5 mm apart, adjusted using a three-axis motion stage) to observe the volumetric flow profile within the aneurysm and along the exit branches. Positions of each cross-sectional scan planes were denoted on the long-axis view movie. Scan planes were positioned to observe flow across the aneurysm midsection, so as to facilitate visualization of the development and progression of flow disturbances from a 4-D (3-D space and time) point of view. Note that all cineloops were time-synchronized to the start of the cardiac cycle, as image acquisition was triggered by the external sync pulse generated by the flow pump system. At the bottom of  Movie 1, a Doppler spectrogram (range gate placed at yellow box) is plotted to correlate the CESI frames to its instantaneous cardiac phase; the temporal position of the cineloops is marked with a sliding yellow line on the spectrogram.

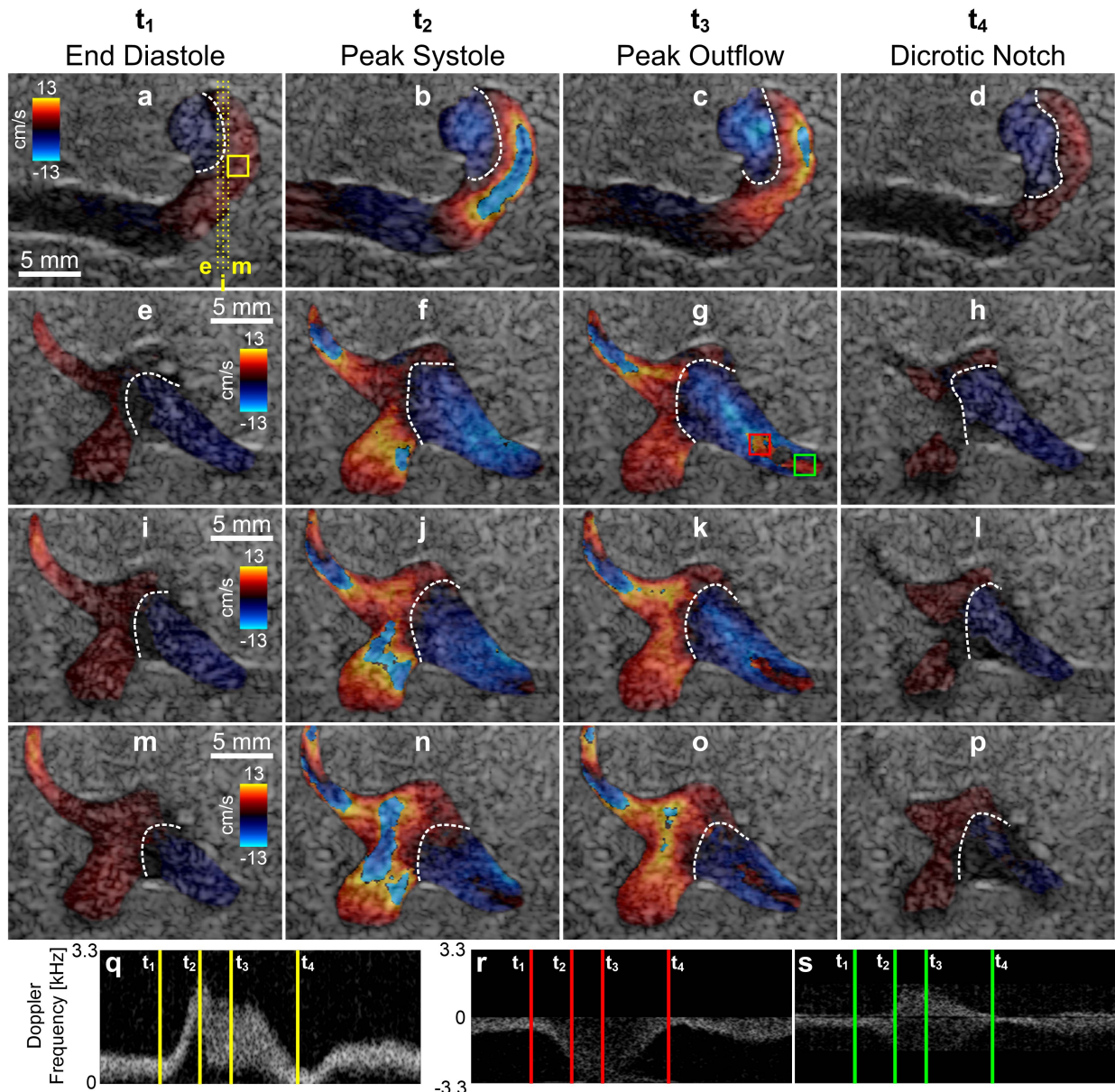


Fig. 8. Still images captured from the Movie 1. The top four rows show the still images of the scan planes in Movie 1 from 1a to 1d, respectively, captured at different time points ( $t_1$ – $t_4$ ). Time  $t_1$ – $t_4$  are time instants at the end of diastole, peak systole, peak outflow, and dicrotic notch, respectively. The bottom row shows the Doppler spectrograms, with range gates placed at (q) ICA inlet marked on (a), and (r) and (s) MCA outlet marked on (g). The flow separation lines are highlighted in all still images with white dashed lines. The scan-plane positions of each cross-sectional view are depicted in (a) using yellow dashed line. Note that the baseline of Doppler spectrogram (q) is at the bottom, while those of (r) and (s) are at the middle.

In general, the flow dynamics shown in Movie 1 are in line with what is to be expected: flow entered the aneurysm from the ICA inlet, recirculated at the aneurysm, and then diverged into the two MCA and PCA exit branches. One key dynamic event that can be observed is that the recirculation vortex inside the aneurysm did not dissipate over a cardiac cycle and persisted until the next cardiac cycle. Another key observation is that the vortex center shifted in position at different cardiac phases; the diastolic vortex moved closer to the anterior of the aneurysm as the swirling motion weakened during end diastole. This phenomenon indicates the formation of a non-axisymmetric vortex, and it is likely attributed to the two non-mirroring exit branches at the flow model.

### E. Still-Frame Rendering of Intraaneurysm Flow Dynamics

To further analyze the flow dynamics within the aneurysm, distinct time points of the cineloop were identified and rendered as still frames in Fig. 8. The first row of Fig. 8 shows frames from the long-axis view while the second, third, and fourth rows, respectively, show frames from the scan planes in Movies 1b–1d. Time points depicting end diastole, peak systole, peak outflow, and dicrotic notch are, respectively, identified from the Doppler spectrogram, and their corresponding CESI still frames from the four scan planes are arranged onto the same column. For each still frame, the flow separation line, distinguished as the zero velocity line between the velocity maxima of opposite signs, is denoted with a white dashed



line. As shown in Fig. 8(a), the first cross-sectional scan plane (🎬 Movie 1b and 2nd row of Fig. 8) was found to slice through recirculation regions with bidirectional flow, while the second cross-sectional scan plane (🎬 Movie 1c and 3rd row of Fig. 8) was positioned directly at the vortex center passing through the flow separation line; the third scan plane (🎬 Movie 1d and 4th row of Fig. 8) captured only the upward flow (red hue) from the ICA inlet toward the apex of the aneurysm. Correspondingly, the flow velocity rendered agreed well to their positions as the observed downward flow (blue hue) reduced, when the scan plane shifts backward to the posterior end of the aneurysm. Note that flow detection was slightly compromised for the cross-sectional views due to the presence of out-plane flow.

At the MCA outlet, one may notice the change in color encoded velocities during systolic phase ( $t_2$  to  $t_3$ ). To determine if the change was an actual representation of the flow direction, or simply an effect of aliasing, their Doppler signal contents were examined. Two range gates were placed at the MCA outlet, boxed in green and red, as highlighted in Fig. 8(g). Their corresponding Doppler spectrograms were shown in Fig. 8(r) and (s), with the spectrogram baseline placed in the middle to serve as a common reference. In Fig. 8(r), it can be observed that the change in encoded color adjacent to the outlet was due to change in flow direction, as the spectral contents spanned between  $\pm PRF/2$ . On the other hand, the change in encoded color highlighted by the red range gate was because of aliasing as Doppler content spanned mostly from zero to  $-PRF/2$ , as shown in Fig. 8(s). This result corresponds well with the cineloop visualization of 🎬 Movie 1.

It is worth pointing out that the difference in Doppler spectrograms obtained from calibration [see Fig. 6(e)] and ICA inlet [Fig. 8(q)] was due to vessel compliance. In particular, the flow profile changed slightly as the flow phantom acted as an elastic chamber due to the Windkessel effect [42]. Moreover, the downstream flow resistors also contributed to flow dynamics changes in the cerebral flow phantom.

## VI. DISCUSSION

### A. Summary of Methodological Contributions

It has been well recognized that fabricating anatomically realistic flow phantoms for vascular ultrasound studies is not a trivial task [1]. The challenge is even more pronounced when attempting to extend beyond co-planar geometries to vascular structures that are tortuous, branching, and varying in cross section. Endeavors have been taken to fabricate tortuous vascular flow phantoms [15], [24] with mixed success, mainly lacking in acoustic compatibility for ultrasound imaging. In this paper, we have devised a new wall-less tortuous vascular phantom fabrication protocol that is based on the marriage between direct rapid prototyping and investment casting principles. In particular, we have established the engineering protocol on how a flow phantom with tortuous and nonplanar vascular geometries can be designed and fabricated based on CT scans of a patient's vasculature. This process involves

the design of computer models with CAD tools (Fig. 1), vessel core construction by rapid prototyping (Fig. 2), and investment casting (Fig. 3) to produce a vascular phantom with acoustically compatible properties. Note that this engineering protocol is extendable to any arbitrary vascular geometry. The patient-specific intracranial aneurysm model is merely a case demonstration of our new tortuous phantom design framework.

In terms of acoustic compatibility, our choice of material was found to possess physiologically comparable properties, in terms of speed of sound and attenuation coefficient (Section IV-A). In a separate study, we have also characterized the mechanical properties of our PVA cryogel and have confirmed it to be within physiological range [43]. As well, it should be noted that PVA-based phantoms generally have a long expected life time (stability over the course of seven months or longer as reported) [44].

In this paper, we have also provided a pedagogical walk-through on the construction of a supporting flow circuit that comprised a programmable flow pump system (Fig. 4) and in-house fabricated BMF (Fig. 5). The programmability of our setup enables customized flow waveforms to be delivered by the flow pump (Fig. 6); users are no longer restricted to vendor-defined waveforms, thereby enabling investigations to be conducted with different flow profiles (e.g., pulse waveform of brachial artery) according to investigative needs. In addition, the fabrication procedure of BMF has been refined for greater accessibility to academic laboratories, requiring only basic wet-lab facilities and necessary raw materials.

### B. Feasibility of Conducting Imaging Experimentation Using Our New Tortuous Vascular Phantom

As a proof-of-concept demonstration, our exemplar phantom of a patient-specific intracranial aneurysm model was put into operation with our flow circuit, and ultrasound imaging experiments were performed (Fig. 7). The corresponding flow dynamics were imaged using an emerging vascular ultrasound technique called CESI that our group developed earlier [26]. The spatiotemporal evolution of flow patterns inside our aneurysm phantom was rendered using CESI (🎬 Movie 1). Results by-and-large confirmed that the intraaneurysm flow dynamics are 3-D in nature (Fig. 8). In particular, complex flow is observed in the vascular phantom due to its tortuosity and flow branches, and a persistent flow recirculation is seen within the aneurysm lasting throughout an entire cardiac cycle. These observations serve to attest that the tortuous vascular phantoms developed using our reported protocol are applicable to performance investigations of new vascular imaging methods, such as CESI.

From an application standpoint, the tortuous flow phantoms that can be developed from our framework will serve well as experimental test beds for other emerging vascular imaging techniques. One example is vector flow imaging [27], [45], which can be considered as a natural extension of CESI toward quantifying the highly dynamic flow patterns in tortuous vasculature. Our developed phantoms may also be applied to the testing of new hemodynamic estimation methods on



parameters, such as wall shear rate [46] and vorticity [47]. The experimental insights gained from these phantom studies may be readily compared against flow profiles derived from computational fluid dynamics methods [48] or other imaging modalities [49] to validate the efficacy of new vascular ultrasound methods under consideration.

In this paper, the flow dynamics of the tortuous phantom are observed from multiple scan planes and analysis on the vortex is performed by comparing the vortex progression between scan planes. Strictly speaking, such method is inadequate in tracking the highly dynamic flow profile in the tortuous phantom, and more critically, in clinical applications. This is mainly attributed to: 1) lack of spatial information (from only four scan planes) and 2) acquisitions not simultaneously obtained but only time-synchronized using an ECG-gating equivalent method. To gain more comprehensive insights on the spatial temporal dynamics, such as recirculation within the aneurysm, a 4-D (3-D space and time) imaging paradigm could potentially address these technical limitations [30], [31]. In this regards, our tortuous phantom may serve as a test bed for 3-D imaging investigations, such as the development of advanced data acquisition hardware [50], 2-D array transducer design [51], signal processing algorithms [52], and visualization techniques to render flow vectors [45].

### C. Limitations of Methodology

Note that the wall-less vascular phantom design protocol reported in this paper fundamentally cannot produce phantoms that exhibit arterial wall motion comparable to those observed *in vivo*. While the current phantom serves well within the domain of flow-related investigations [8], it is not applicable to arterial wall dynamics studies, such as pressure wave propagation analysis [53] as well as imaging of wall deformation and strain distribution [54]. To extend the reported framework to explicitly include a wall feature, we surmise that a two-part molding strategy [43] can possibly be employed. Along this direction, it will be essential to overcome the inherent challenge associated with the mounting of a tortuous, nonplanar vascular core replicate within an outer mold. If successfully developed, such walled tortuous vascular phantoms can serve well as experimental test beds for studies on the interaction between hemodynamics and arterial wall motion [55].

Regarding limitations of specific steps in our phantom fabrication protocol, one issue to be noted is that the minimum feature size of a developable model is mainly constrained by the resolution of the 3-D printer. Specifically, with the setup available in our laboratory, the smallest lumen size that can be stably fabricated is 1 mm (four times the extruder size of 0.25 mm). On a similar note, structural features, such as branching order and tortuosity, may also be constrained by their proximity with each other, if the printer resolution is insufficient to resolve them. Nonetheless, this limitation will likely become less significant in the future with the advent of more advanced 3-D printing solutions that offer micrometer-scale print resolution.

## VII. CONCLUSION

Vascular flow phantoms with anatomically realistic geometries are crucial for *in vitro* experiments to yield performance findings that are relevant to *in vivo* conditions. In this paper, we have reported a new phantom design protocol on how tortuous phantoms can be designed, and have described the use of this framework to design a patient-specific intracranial aneurysm phantom based on CT-angiogram scans. In addition, we have demonstrated the designed model's potential as an investigative tool for novel vascular flow imaging algorithms. This new design protocol may be readily applied to develop phantoms for different vascular geometries, and, in turn, enable investigations to pursue innovations in ultrasound flow imaging paradigms that track complex hemodynamics, especially in cases with significant flow disturbance due to its tortuous geometry. Other application development efforts in vascular ultrasound may also leverage these tortuous phantoms as calibration and training tools.

## REFERENCES

- [1] P. R. Hoskins, "Simulation and validation of arterial ultrasound imaging and blood flow," *Ultrasound Med. Biol.*, vol. 34, no. 5, pp. 693–717, May 2008.
- [2] J. E. Browne, "A review of Doppler ultrasound quality assurance protocols and test devices," *Phys. Medica*, vol. 30, no. 7, pp. 742–751, Nov. 2014.
- [3] U. Jaffer, P. Normahani, P. Singh, M. Aslam, and N. J. Standfield, "The effect of a simulation training package on skill acquisition for duplex arterial stenosis detection," *J. Surgical Edu.*, vol. 72, no. 2, pp. 310–315, Mar. 2015.
- [4] E. Y. Wong, H. N. Nikolov, M. L. Thorne, T. L. Poepping, R. N. Rankin, and D. W. Holdsworth, "Clinical Doppler ultrasound for the assessment of plaque ulceration in the stenosed carotid bifurcation by detection of distal turbulence intensity: A matched model study," *Eur. Radiol.*, vol. 19, pp. 2739–2749, Jun. 2009.
- [5] C. H. Leow, E. Bazigou, R. J. Eckersley, A. C. H. Yu, P. D. Weinberg, and M. X. Tang, "Flow velocity mapping using contrast enhanced high-frame-rate plane wave ultrasound and image tracking: Methods and initial *in vitro* and *in vivo* evaluation," *Ultrasound Med. Biol.*, vol. 41, no. 11, pp. 2913–2925, Nov. 2015.
- [6] R. K. Warriner, K. W. Johnston, and R. S. C. Cobbold, "A viscoelastic model of arterial wall motion in pulsatile flow: Implications for Doppler ultrasound clutter assessment," *Physiol. Meas.*, vol. 29, no. 2, pp. 157–180, Feb. 2008.
- [7] A. Swillens, L. Løvstakken, J. Kips, H. Torp, and P. Segers, "Ultrasound simulation of complex flow velocity fields based on computational fluid dynamics," *IEEE Trans. Ultrason., Ferroelect., Freq. Control*, vol. 56, no. 3, pp. 546–556, Mar. 2009.
- [8] D. W. Rickey, P. A. Picot, D. A. Christopher, and A. Fenster, "A wall-less vessel phantom for Doppler ultrasound studies," *Ultrasound Med. Biol.*, vol. 21, no. 9, pp. 1163–1176, Sep. 1995.
- [9] K. V. Ramnarine, T. Anderson, and P. R. Hoskins, "Construction and geometric stability of physiological flow rate wall-less stenosis phantoms," *Ultrasound Med. Biol.*, vol. 27, no. 2, pp. 245–250, Feb. 2001.
- [10] S. F. C. Stewart, "A rotating torus phantom for assessing color Doppler accuracy," *Ultrasound Med. Biol.*, vol. 25, no. 8, pp. 1251–1264, Aug. 2001.
- [11] A. Walker, E. Henriksen, I. Ringqvist, and P. Ask, "A rotating cylinder phantom for flow and tissue color Doppler testing," *Ultrasound Med. Biol.*, vol. 35, no. 11, pp. 1892–1898, Nov. 2009.
- [12] S. Courane, A. J. Fagan, and J. E. Browne, "An audit of a hospital-based Doppler ultrasound quality control protocol using a commercial string Doppler phantom," *Phys. Medica*, vol. 30, no. 3, pp. 380–384, May 2014.
- [13] T. L. Poepping, H. N. Nikolov, R. N. Rankin, M. Lee, and D. W. Holdsworth, "An *in vitro* system for Doppler ultrasound flow studies in the stenosed carotid artery bifurcation," *Ultrasound Med. Biol.*, vol. 28, no. 4, pp. 495–506, Apr. 2002.

- [14] D. M. King, M. Ring, C. M. Moran, and J. E. Browne, "Development of a range of anatomically realistic renal artery flow phantoms," *Ultrasound Med. Biol.*, vol. 36, no. 7, pp. 1135–1144, Jul. 2010.
- [15] T. L. Poepping, H. N. Nikolov, M. L. Thorne, and D. W. Holdsworth, "A thin-walled carotid vessel phantom for Doppler ultrasound flow studies," *Ultrasound Med. Biol.*, vol. 30, no. 3, pp. 1067–1078, Mar. 2004.
- [16] D. M. King, C. M. Moran, J. D. McNamara, A. J. Fagan, and J. E. Browne, "Development of a vessel-mimicking material for use in anatomically realistic Doppler flow phantoms," *Ultrasound Med. Biol.*, vol. 37, no. 5, pp. 813–826, May 2011.
- [17] L. Allard, G. Soulez, B. Chayer, Z. Qin, D. Roy, and G. Cloutier, "A multimodality vascular imaging phantom of an abdominal aortic aneurysm with a visible thrombus," *Med. Phys.*, vol. 40, no. 6, p. 063701, Jun. 2013.
- [18] D. M. Watts, C. J. Sutcliffe, R. N. Morgan, S. Meagher, J. Wardlaw, M. Connell, M. E. Bastin, I. Marshall, K. V. Ramnarine, P. R. Hoskins, and R. A. Black, "Anatomical flow phantoms of the nonplanar carotid bifurcation, part I: Computer-aided design and fabrication," *Ultrasound Med. Biol.*, vol. 33, no. 2, pp. 296–302, Feb. 2007.
- [19] S. Meagher, T. L. Poepping, K. V. Ramnarine, R. A. Black, and P. R. Hoskins, "Anatomical flow phantoms of the nonplanar carotid bifurcation, part II: Experimental validation with Doppler ultrasound," *Ultrasound Med. Biol.*, vol. 33, no. 2, pp. 303–310, Feb. 2007.
- [20] A. Sulaiman, C. Roty, J. M. Serfaty, C. Attia, L. Huet, and P. Douek, "In vitro, nonrigid model of aortic arch aneurysm," *J. Vascular Interventional Radiol.*, vol. 19, no. 6, pp. 919–924, Jun. 2008.
- [21] G. Biglino, P. Verschuere, R. Zegels, A. M. Taylor, and S. Schievano, "Rapid prototyping compliant arterial phantoms for in-vitro studies and device testing," *J. Cardiovascular Mag. Reson.*, vol. 15, no. 1, p. 2, Jan. 2013.
- [22] E. Y. Wong, M. L. Thorne, H. N. Nikolov, T. L. Poepping, and D. W. Holdsworth, "Doppler ultrasound compatible plastic material for use in rigid flow models," *Ultrasound Med. Biol.*, vol. 34, no. 11, pp. 1846–1856, Nov. 2008.
- [23] S. S. M. Lai, B. Y. S. Yiu, A. K. K. Poon, and A. C. H. Yu, "Design of anthropomorphic flow phantoms based on rapid prototyping of compliant vessel geometries," *Ultrasound Med. Biol.*, vol. 39, no. 9, pp. 1654–1664, Sep. 2013.
- [24] A. C. O. Tsang, S. S. M. Lai, W. C. Chung, A. Y. S. Tang, G. K. K. Leung, A. K. K. Poon, A. C. H. Yu, and K. W. Chow, "Blood flow in intracranial aneurysms treated with pipeline embolization devices: Computational simulation and verification with Doppler ultrasonography on phantom models," *Ultrasonography*, vol. 34, no. 2, pp. 98–108, Apr. 2015.
- [25] J. Bercoff, G. Montaldo, T. Loupas, D. Savary, F. Meziere, M. Fink, and M. Tanter, "Ultrafast compound Doppler imaging: Providing full blood flow characterization," *IEEE Trans. Ultrason., Ferroelect., Freq. Control*, vol. 58, no. 1, pp. 134–147, Jan. 2011.
- [26] B. Y. S. Yiu and A. C. H. Yu, "High-frame-rate ultrasound color-encoded speckle imaging of complex flow dynamics," *Ultrasound Med. Biol.*, vol. 39, no. 6, pp. 1015–1025, Jun. 2013.
- [27] B. Y. S. Yiu, S. S. M. Lai, and A. C. H. Yu, "Vector projectile imaging: Time-resolved dynamic visualization of complex flow patterns," *Ultrasound Med. Biol.*, vol. 40, no. 9, pp. 2295–2309, Sep. 2014.
- [28] C. Tremblay-Darveau, R. Williams, L. Milot, M. Bruce, and P. N. Burns, "Combined perfusion and doppler imaging using plane-wave nonlinear detection and microbubble contrast agents," *IEEE Trans. Ultrason., Ferroelect., Freq. Control*, vol. 61, no. 12, pp. 1988–2000, Dec. 2014.
- [29] I. K. Ekroll, M. M. Voormolen, O. K.-V. Standal, J. M. Rau, and L. Lovstakken, "Coherent compounding in Doppler imaging," *IEEE Trans. Ultrason., Ferroelect., Freq. Control*, vol. 62, no. 9, pp. 1634–1643, Sep. 2015.
- [30] M. J. Pihl and J. A. Jensen, "A transverse oscillation approach for estimation of three-dimensional velocity vectors, part I: Concept and simulation study," *IEEE Trans. Ultrason., Ferroelect., Freq. Control*, vol. 61, no. 10, pp. 1599–1607, Oct. 2014.
- [31] M. J. Pihl, M. B. Stuart, B. G. Tomov, M. F. Rasmussen, and J. A. Jensen, "A transverse oscillation approach for estimation of three-dimensional velocity vectors. Part II: Experimental validation," *IEEE Trans. Ultrason., Ferroelect., Freq. Control*, vol. 61, no. 10, pp. 1608–1618, Oct. 2014.
- [32] D. M. Sforza, C. M. Putman, and J. R. Cebra, "Hemodynamics of cerebral aneurysms," *Annu. Rev. Fluid Mech.*, vol. 41, pp. 91–107, Jan. 2009.
- [33] G. Byrne, F. Mut, and J. Cebra, "Quantifying the large-scale hemodynamics of intracranial aneurysms," *Amer. J. Neuroradiol.*, vol. 35, no. 2, pp. 335–338, Feb. 2014.
- [34] K. J. M. Surry, H. J. B. Austin, A. Fenster, and T. M. Peters, "Poly(vinyl alcohol) cryogel phantoms for use in ultrasound and MR imaging," *Phys. Med. Biol.*, vol. 49, no. 24, pp. 5529–5546, Dec. 2004.
- [35] K. V. Ramnarine, D. K. Nassiri, P. R. Hoskins, and J. Lubbers, "Validation of a new blood-mimicking fluid for use in Doppler flow test objects," *Ultrasound Med. Biol.*, vol. 24, no. 3, pp. 451–459, Mar. 1998.
- [36] K. Zell, J. I. Sperl, M. W. Vogel, R. Niessner, and C. Haisch, "Acoustical properties of selected tissue phantom materials for ultrasound imaging," *Phys. Med. Biol.*, vol. 52, no. 20, pp. N475–N494, Oct. 2007.
- [37] P. R. Hoskins, "Physical properties of tissues relevant to arterial ultrasound imaging and blood velocity measurement," *Ultrasound Med. Biol.*, vol. 33, no. 10, pp. 1527–1539, Oct. 2007.
- [38] S. Kefayati, D. W. Holdsworth, and T. L. Poepping, "Turbulence intensity measurements using particle image velocimetry in diseased carotid artery models: Effect of stenosis severity, plaque eccentricity, and ulceration," *J. Biomech.*, vol. 47, no. 1, pp. 253–263, Jan. 2014.
- [39] C. C. P. Cheung, A. C. H. Yu, N. Salimi, B. Y. S. Yiu, I. K. H. Tsang, B. Kerby, R. Z. Azar, and K. Dickie, "Multi-channel pre-beamformed data acquisition system for research on advanced ultrasound imaging methods," *IEEE Trans. Ultrason., Ferroelect., Freq. Control*, vol. 59, no. 2, pp. 243–253, Feb. 2012.
- [40] H. So, J. Chen, B. Y. S. Yiu, and A. C. H. Yu, "Medical ultrasound imaging: To GPU or not to GPU?" *IEEE Micro*, vol. 31, no. 5, pp. 54–65, Sep. 2011.
- [41] B. Y. S. Yiu, I. K. H. Tsang, and A. C. H. Yu, "GPU-based beamformer: Fast realization of plane wave compounding and synthetic aperture imaging," *IEEE Trans. Ultrason., Ferroelect., Freq. Control*, vol. 58, no. 8, pp. 1698–1705, Aug. 2011.
- [42] Y. C. Fung, *Biomechanics: Mechanical Properties of Living Tissues*, 2nd ed. New York, NY, USA: Springer-Verlag, 1993, p. 21.
- [43] A. J. Y. Chee, C. K. Ho, B. Y. S. Yiu, and A. C. H. Yu, "Walled carotid bifurcation phantoms for imaging investigations of vessel wall motion and blood flow dynamics," *IEEE Trans. Ultrason., Ferroelect., Freq. Control*, vol. 63, no. 11, pp. 1852–1864, Nov. 2016.
- [44] F. Duboeuf, A. Basarab, H. Liebgott, E. Brusseau, P. Delachartre, and D. Vray, "Investigation of PVA cryogel Young's modulus stability with time, controlled by a simple reliable technique," *Med. Phys.*, vol. 36, no. 2, pp. 656–661, Feb. 2009.
- [45] J. A. Jensen, S. I. Nikolov, A. C. H. Yu, and D. Garcia, "Ultrasound vector flow imaging—Part II: Parallel systems," *IEEE Trans. Ultrason., Ferroelect., Freq. Control*, vol. 63, no. 11, pp. 1722–1732, Nov. 2016.
- [46] D. W. Park, G. H. Kruger, J. M. Rubin, J. Hamilton, J. Gottschalk, R. E. Dodde, A. J. Shih, and W. F. Weitzel, "Quantification of ultrasound correlation-based flow velocity mapping and edge velocity gradient measurement," *J. Ultrasound Med.*, vol. 32, no. 10, pp. 1815–1830, Oct. 2013.
- [47] F. Mehregan, F. Tournoux, S. Muth, P. Pibarot, R. Rieu, G. Cloutier, and D. Garcia, "Doppler vortography: A color Doppler approach to quantification of intraventricular blood flow vortices," *Ultrasound Med. Biol.*, vol. 40, no. 1, pp. 210–221, Jan. 2014.
- [48] J. V. Cauwenberge, L. Lovstakken, S. Fadnes, A. Rodriguez-Morales, J. Vierendeels, P. Segers, and A. Swillens, "Assessing the performance of ultrafast vector flow imaging in the neonatal heart via multiphysics modeling and in vitro experiments," *IEEE Trans. Ultrason., Ferroelect., Freq. Control*, vol. 63, no. 11, pp. 1772–1785, Nov. 2016.
- [49] D. Thakrar, A. Popescu, S. Gupta, A. de Freitas, H. Russell, J. Carr, and M. Markl, "Complex 3D blood flow pathways in two cases of aorta to right heart fistulae: A 4D flow MRI study," *Magn. Reson. Imag.*, vol. 31, no. 8, pp. 1453–1455, Oct. 2013.
- [50] J. A. Jensen, M. F. Holtén-Lund, R. T. Nilsson, M. Hansen, U. D. Larsen, R. P. Domsten, B. G. Tomov, M. B. Stuart, S. I. Nikolov, M. J. Pihl, Y. Du, J. H. Rasmussen, and M. F. Rasmussen, "SARUS: A synthetic aperture real-time ultrasound system," *IEEE Trans. Ultrason., Ferroelect., Freq. Control*, vol. 60, no. 9, pp. 1838–1852, Sep. 2013.
- [51] E. Roux, A. Ramalli, P. Tortoli, C. Cachard, M. Robini, and H. Liebgott, "2-D ultrasound sparse arrays multiplexed radiation optimization using simulated annealing and spiral-array inspired energy functions," *IEEE Trans. Ultrason., Ferroelect., Freq. Control*, vol. 63, no. 12, pp. 2138–2149, Dec. 2016.
- [52] B. Hussain, B. Y. S. Yiu, A. C. H. Yu, J. C. Laceyfield, and T. L. Poepping, "Investigation of crossbeam multi-receiver configurations for accurate 3-D vector doppler velocity estimation," *IEEE Trans. Ultrason., Ferroelect., Freq. Control*, vol. 63, no. 11, pp. 1786–1798, Nov. 2016.

- [53] J. Luo, R. X. Li, and E. E. Konofagou, "Pulse wave imaging of the human carotid artery: An *in vivo* feasibility study," *IEEE Trans. Ultrason., Ferroelect., Freq. Control*, vol. 59, no. 1, pp. 174–181, Jan. 2012.
- [54] M. Larsson, B. Heyde, F. Kremer, L. Brodin, and J. D'hooge, "Ultrasound speckle tracking for radial, longitudinal and circumferential strain estimation of the carotid artery—An *in vitro* validation via sonomicrometry using clinical and high-frequency ultrasound," *Ultrasonics*, vol. 56, pp. 399–408, Feb. 2015.
- [55] I. K. Ekroll, A. Swillens, P. Segers, T. Dahl, H. Torps, and L. Lovstakken, "Simultaneous quantification of flow and tissue velocities based on multi-angle plane wave imaging," *IEEE Trans. Ultrason., Ferroelect., Freq. Control*, vol. 60, no. 4, pp. 727–739, Apr. 2013.



**Chung Kit Ho** graduated from the Medical Engineering Program at the University of Hong Kong with the B.Eng. (Hons) degree in 2014. After a brief industry work experience, he returned to the University of Hong Kong in 2015 to work as a Research Engineer in the Biomedical Ultrasound Laboratory. He will soon become an M.A.Sc. student at the University of Waterloo, ON, Canada. His research is presently focused on designing novel vascular phantoms for ultrasound imaging investigations.



**Adrian J. Y. Chee** (GS'09) was born in Malaysia. He received the B.Eng. degree (with first class honors) in electrical and computer systems engineering from Monash University, Melbourne, Australia, in 2011. He then received the Ph.D. degree from the University of Hong Kong in 2016.

He was a research intern at Hitachi Central Research Laboratory, Tokyo, Japan, in 2016. He will soon become a Postdoctoral Fellow at the University of Waterloo, ON, Canada. His current research is focused on the design of new ultrasound-based

vascular diagnostic techniques and related experimental tools.

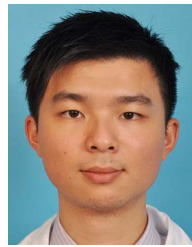


**Billy Y. S. Yiu** (M'10) was born and raised in Hong Kong. He is now working as a Research Scientist in the Biomedical Ultrasound Laboratory at the University of Hong Kong. He received the B.Eng. (Hons) degree in medical engineering in 2007, and completed the M.Phil. degree in electrical and electronic engineering in 2010, both at the University of Hong Kong.

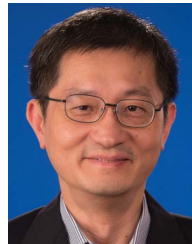
His current research interest is in advanced ultrasound imaging, specifically in the design of high-frame-rate imaging techniques and related system

tools.

Mr. Yiu was the recipient of the Young Scientist Award at the 2013 Symposium on Ultrasonic Electronics and the Young Investigator Gold Prize Award at the 2014 KSUM Annual Convention.



**Anderson C. O. Tsang** is a neurosurgeon and Clinical Assistant Professor at the Division of Neurosurgery, The University of Hong Kong. He received the M.B.B.S. degree from the University of Hong Kong in 2010, after which he joined the Department of Surgery at Queen Mary Hospital where he received training in neurosurgery. His research interests focused on cerebrovascular disease and clinical neurosurgery, in particular cerebral aneurysms treatment and flow dynamics.



**Kwok Wing Chow** received the bachelor's degree from the California Institute of Technology, Pasadena, CA, USA, and the Ph.D. degree from the Massachusetts Institute of Technology, Cambridge, MA, USA.

He taught at the University of Arizona, Tucson, AZ, USA for a few years before settling at the University of Hong Kong (HKU). He is currently a Professor of Mechanical Engineering at HKU. His research interests include fluid mechanics, medical engineering and wave propagation.



**Alfred C. H. Yu** (S'99–M'07–SM'12) received the undergraduate degree in electrical engineering from the University of Calgary, AB, Canada, in 2002, and the M.A.Sc. and Ph.D. degrees in biomedical engineering from the University of Toronto, ON, Canada, in 2004 and 2007, respectively.

He is an Associate Professor in the Department of Electrical and Computer Engineering at the University of Waterloo, ON, Canada. He has a long-standing research interest in ultrasound imaging innovations and therapeutic ultrasound discoveries.

He was an intern at Philips Research North America, Briarcliff Manor, NY, USA, in 2005. Before he relocated to Waterloo, Prof. Yu was a Research Assistant Professor at the University of Hong Kong, where he founded and served as the Principal Investigator of HKU Biomedical Ultrasound Laboratory.

Prof. Yu is the recipient of the 2016 IEEE Ultrasonics Early Career Investigator Award. He is a Senior Member of AIUM. He is an Associate Editor of IEEE TRANSACTIONS ON ULTRASONICS, FERROELECTRICS, AND FREQUENCY CONTROL and an Editorial Board Member of *Ultrasound in Medicine and Biology*. He also serves on the Technical Program Committee of *IEEE Ultrasonics Symposium* and *International Symposium for Therapeutic Ultrasound*.